

## Two stable methods with numerical experiments for solving the backward heat equation

Fabien Ternat<sup>a</sup>, Oscar Orellana<sup>b</sup>, Prabir Daripa<sup>c,\*</sup>

<sup>a</sup> Institut de Recherche sur les Phénomènes Hors-Équilibre, IRPHE, Marseille, France

<sup>b</sup> Departamento de matemáticas, Universidad Técnica Santa María de Valparaíso, UTFSM, Chile

<sup>c</sup> Department of Mathematics, Texas A&M University, College Station, TX, United States

### ARTICLE INFO

#### Article history:

Received 3 December 2009

Received in revised form 17 July 2010

Accepted 9 September 2010

Available online 14 October 2010

#### Keywords:

Backward heat equation

Ill-posed problem

Numerical methods

Crank–Nicolson method

Euler scheme

Dispersion relation

Filtering

Regularization

### ABSTRACT

This paper presents results of some numerical experiments on the backward heat equation. Two quasi-reversibility techniques, explicit filtering and structural perturbation, to regularize the ill-posed backward heat equation have been used. In each of these techniques, two numerical methods, namely Euler and Crank–Nicolson (CN), have been used to advance the solution in time.

Crank–Nicolson method is very counter-intuitive for solving the backward heat equation because the dispersion relation of the scheme for the backward heat equation has a singularity (unbounded growth) for a particular wave whose finite wave number depends on the numerical parameters. In comparison, the Euler method shows only catastrophic growth of relatively much shorter waves. Strikingly we find that use of smart filtering techniques with the CN method can give as good a result, if not better, as with the Euler method which is discussed in the main text. Performance of these regularization methods using these numerical schemes have been exemplified.

© 2010 IMACS. Published by Elsevier B.V. All rights reserved.

### 1. Introduction

The problem of heat conduction through a conducting medium occupying a space  $\Omega$  subject to no heat flux across the boundary of the region is formulated as follows:

$$\begin{cases} u_t - \nu u_{xx} = 0, & x \in \Omega, t > 0, \\ u_x|_{\partial\Omega} = 0, & t > 0, \\ u(x, 0) = u_0(x), & x \in \Omega. \end{cases} \quad (1)$$

Here  $u(x, t)$  is the temperature and  $u_0(x)$  is the initial temperature distribution. This problem is known to be well-posed in the sense of Hadamard, i.e. existence, uniqueness and continuous dependence of the solution on the boundary data are well-established for this problem. The above problem is usually referred as a forward problem in the context of heat equation.

The backward problem related to the heat equation refers to the problem of finding the initial temperature distribution of the forward problem from a knowledge of the final temperature distribution  $v_0(x)$  at time  $T$ :

\* Corresponding author.

E-mail address: prabir.daripa@math.tamu.edu (P. Daripa).

$$\begin{cases} u_t - \nu u_{xx} = 0, & x \in \Omega, t \in [0, T], \\ u_x|_{\partial\Omega} = 0, \\ u(x, T) = v_0(x), & x \in \Omega. \end{cases} \tag{2}$$

The change of variable  $t \rightarrow T - t$  leads to the following formulation of this backward problem where  $v(x, t) = u(x, T - t)$ :

$$\begin{cases} v_t + \nu v_{xx} = 0, & x \in \Omega, t \in [0, T], \\ v_x|_{\partial\Omega} = 0, \\ v(x, 0) = v_0(x), & x \in \Omega. \end{cases} \tag{3}$$

This backward problem is ill-posed on all three counts: existence, uniqueness and continuous dependence of solution on arbitrary initial data (see Nash [19], John [11], Miranker [17] and Hollig [9]), though this problem is well-posed for initial data whose Fourier spectrum has compact support (see Miranker [17]). However, in practice, an initial data cannot in general be guaranteed to have a compact support in Fourier space. When an initial data has a compact support in Fourier space, it loses this compactness in practice for a variety of reasons such as measurement error, noise in the measured data, round-off error in machine representations of such data, just to mention a few reasons. Integrating such equations by any numerical scheme further compounds this problem due to the effect of truncation error. Because of these reasons, even when a unique solution of the backward problem exists for some particular initial data, computing such a solution in some stable way has been a challenge for a long time (see Douglas and Gallie [6], John [11], Pucci [20]).

A constructive approach to circumvent this computational challenge is to analyze first the dispersion relation. The dispersion relation associated with the backward heat equation is  $\omega = k^2$ , i.e. a mode with wave number  $k$  grows quadratically. This kind of catastrophic growth of short waves is also an indication that solutions (classical) of the backward problem may not always exist for all time for arbitrary initial data. This is all too well known for the backward heat equation for we know that any discontinuous temperature profile gets smoothed out instantaneously by forward heat equation. Another consequence of this is the undesirable catastrophic growth of errors (in particular in high wave number modes) arising due to numerical approximation of the equation (truncation error), the machine representation of the data (roundoff error) and noise in any measured data.

In this paper, computation of solutions of this ill-posed backward heat equation is undertaken on appropriately chosen space–time grid in conjunction with filtering and regularization techniques. We present numerical results that show that solutions can be computed in stable ways for times longer than earlier reported by clever choice of the grids, filters, regularization term and clever dynamic application of the chosen filters. We also present detail outline of the procedures so that the computational results presented here can be reproduced by anyone interested in doing so. It is worth pointing out here that the filtering techniques reported earlier in the literature with other ill-posed problems (see [13,22,4,5,8]) have been applied here successfully to this backward heat problem.

## 2. Numerical schemes and results

The computational domain  $\Omega$  is taken to be one dimensional, in particular  $\Omega = [0, 1]$ . We discretize the interval  $[0, 1]$  with  $M$  subintervals  $\Delta x = 1/M$  of equal length with grid points denoted by  $x_m, m = 0, \dots, M$ . Integration in time is done in time step of  $\Delta t$  with time interval  $T = N \times \Delta t$  and  $t_n = n \times \Delta t, n = 0, \dots, N$ . The exact value of the solution at  $(x_m, t_n)$  is denoted by  $v(x_m, t_n)$  and numerical value by  $v_m^n$ . Zero Neumann boundary conditions at both end points of the interval  $[0, 1]$  are approximated that results in the following third order accurate end point values of  $v$  for  $t > 0$ ,

$$v(0, t) = \frac{4v(\Delta x, t) - v(2\Delta x, t)}{3} + O((\Delta x)^3), \tag{4}$$

$$v(1, t) = \frac{4v(1 - \Delta x, t) - v(1 - 2\Delta x, t)}{3} + O((\Delta x)^3). \tag{5}$$

### 2.1. Euler scheme

In terms of forward and backward finite difference operators  $D^+$  and  $D^-$ , the finite difference equation for the backward heat equation is

$$\frac{D_t^+ v_m^n}{\Delta t} = -\nu \frac{D_x^+ D_x^- v_m^n}{\Delta x^2}, \quad \forall m \neq \{1, M\}, \quad \forall n > 2. \tag{6}$$

For numerical construction of solutions, it is useful to choose appropriate values of  $\Delta x$  and  $\Delta t$  so that numerical and exact dispersion relations do not deviate too much from each other over a range of participating wave numbers. Using the ansatz  $v_m^n = \rho^n e^{i\xi m}$  (where  $\rho = e^{\beta \Delta t}$  and  $\xi = k\pi \Delta x$ ) in the finite difference equation (6) yields the dispersion relation,

$$\rho = 1 + 4\nu r \sin^2(k\pi \Delta x/2), \tag{7}$$

where  $r = \Delta t/\Delta x^2$ . When  $\Delta x \rightarrow 0$ , we have  $\rho \sim 1 + (k\pi)^2 \nu \Delta t$  which gives, in the limit  $\Delta t \rightarrow 0, \beta = \ln |\rho|/\Delta t \sim \nu(k\pi)^2$  which is same as the exact growth rate.

## 2.2. Crank–Nicolson scheme

The backward heat equation in this scheme is discretized as

$$\frac{D_t^+ v_m^n}{\Delta t} = -\frac{\nu}{2\Delta x^2} (D_x^+ D_x^- v_m^{n+1} + D_x^+ D_x^- v_m^n). \quad (8)$$

For dispersion relation, same ansatz for  $v_m^n$  as in the Euler scheme is inserted in the finite difference equation (8). This yields the following dispersion relation

$$\rho = \frac{1 + 2\nu r \sin^2\left(\frac{\xi}{2}\right)}{1 - 2\nu r \sin^2\frac{\xi}{2}}, \quad (9)$$

where  $r = \Delta t/\Delta x^2$  as before. When  $\Delta x \rightarrow 0$ , we have

$$\rho \sim \frac{1 + \nu(k\pi)^2 \frac{\Delta t}{2}}{1 - \nu(k\pi)^2 \frac{\Delta t}{2}},$$

which gives, in the limit  $\Delta t \rightarrow 0$ ,  $\beta = \ln|\rho|/\Delta t \sim \nu(k\pi)^2$  which is the same as the exact dispersion relation. For  $r > 1/2\nu$ , the dispersion relation has a singularity at  $k = k_u$  given by

$$k_u = \frac{2}{\pi \Delta x} \arcsin\left(\frac{\Delta x}{\sqrt{2\nu \Delta t}}\right). \quad (10)$$

Figs. 1(a) and 1(b) compare the exact dispersion relation with the numerical ones for several values of space and time steps respectively for both the Euler and the CN schemes. The plots are log–log plots due to the large values of growth rates. Numerical dispersion plot for the CN scheme corresponding to  $\Delta x = 10^{-3}$  and  $\Delta t = 10^{-4}$  for which  $r > 1/2\nu$  clearly shows the location of the singularity at  $k_u = 45.05$ . Since the singularity and high values of the growth rate are very localized near a very high wave number with rest of the dispersion curves comparing favorably with the exact one, larger time steps may still be able to yield reasonably accurate solutions on the same grid  $\Delta x$  as for the other dispersion curves in the figure. We will test below whether this is indeed true or not. For the other choices of grid values used for the CN case in the figure,  $r$  is less than  $1/2$  ( $r < 1/2\nu$ ). This figure shows that numerical dispersion curves compare favorably with the exact one up to a higher wave number for the CN scheme than for the Euler scheme. However, they all are almost same for up to a wave number approximately 25.

## 2.3. Numerical results

Numerical experiments have been performed on many problems but the results from the ones corresponding to only the following problems are presented below for brevity.

**Example 1** (*Single cosine mode*). It is easy to see that the function

$$v_e(x, t) = \cos(k\pi x) \exp(-k^2 \pi^2 \nu (T_0 - t)), \quad (11)$$

is the solution of the backward heat equation with initial data

$$v_0(x) = \cos(k\pi x) \exp(-k^2 \pi^2 \nu T_0). \quad (12)$$

Note that  $v_x(x, t) = 0$  at  $x = 0, 1$  for all  $t > 0$ .

**Example 2** (*Gaussian*). It is easy to check that

$$v(x, t) = \frac{1}{\sqrt{5-4t}} \exp\left(-\frac{(x-0.5)^2}{\nu(5-4t)}\right), \quad 0 \leq t \leq 1, \quad (13)$$

is the solution of the backward heat equation with initial data

$$v(x, 0) = \frac{1}{\sqrt{5}} \exp\left(-\frac{(x-0.5)^2}{5\nu}\right). \quad (14)$$

It follows that

$$v_x(x, t) = \frac{-2(x-0.5)}{\nu(5-4t)^{3/2}} \exp\left(-\frac{(x-0.5)^2}{\nu(5-4t)}\right), \quad 0 \leq t \leq 1,$$

which is not exactly zero at the end points. It can be made close to zero by choosing a small value of  $\nu$ .

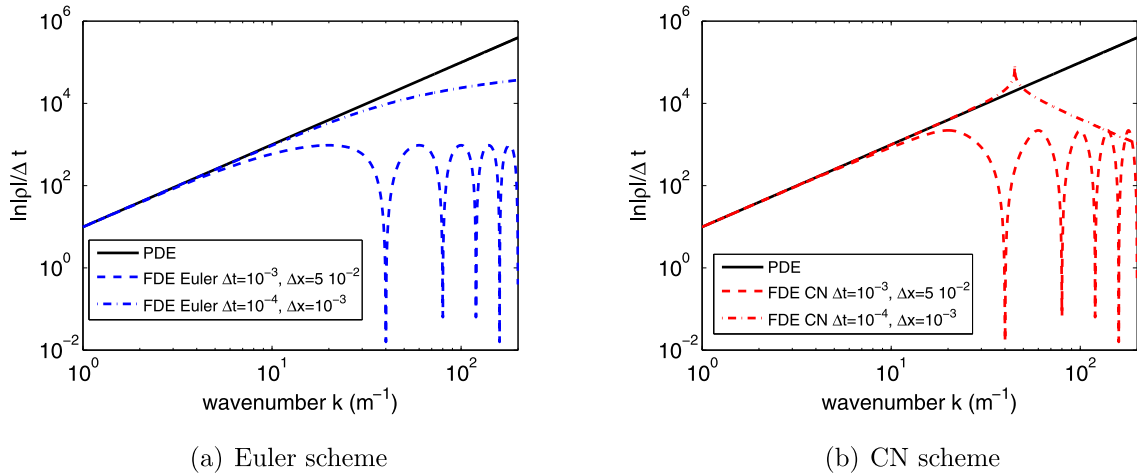


**Fig. 1.** Comparison (in log scale) of the exact dispersion relations of the Euler and Crank–Nicolson schemes for various values of space and time steps. FDE stands for “Finite Difference Equation”. Note the singularity at  $k_i = 45.05$  in the Crank–Nicolson FDE for  $\Delta t = 10^{-4}$  and  $\Delta x = 10^{-3}$ .

**Example 3 (Square bump).** This function is given by

$$h(x) = \begin{cases} 0, & 0 < x < 1/4, \\ 1, & 1/4 < x < 3/4, \\ 0, & 3/4 > x > 1. \end{cases} \tag{15}$$

The exact solution of the forward problem with this square bump initial data is given by

$$u(x, t) = a_0 + \sum_{k=1}^{\infty} a_k \cos(k\pi x) e^{-\nu k^2 \pi^2 t},$$

where

$$a_0 = 1/2, \quad a_k = \frac{2}{k\pi} \left( \sin \frac{3k\pi}{4} - \sin \frac{k\pi}{4} \right), \quad k \geq 1.$$

It then follows that the exact solution of the backward heat equation with initial data

$$v(x, 0) = a_0 + \sum_{k=1}^{\infty} a_k \cos(k\pi x) e^{-\nu k^2 \pi^2 T_0}, \tag{16}$$

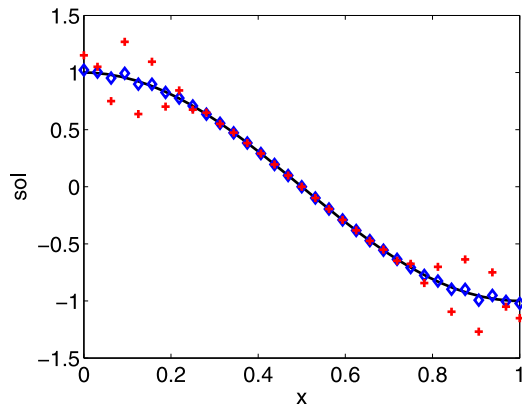
is given by

$$v(x, t) = a_0 + \sum_{k=1}^{\infty} a_k \cos(k\pi x) e^{-\nu k^2 \pi^2 (T_0 - t)}, \quad 0 \leq t \leq T_0.$$

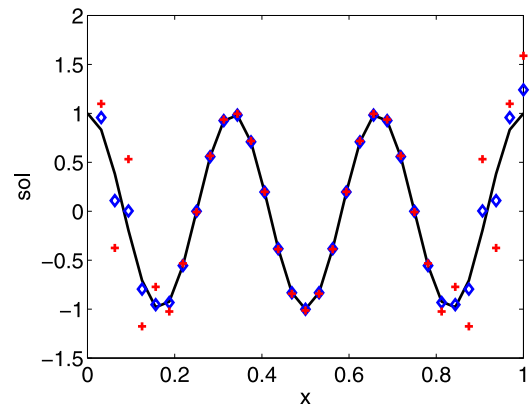
It is found that fifty modes are more than sufficient to accurately represent the bump function (15). Therefore, the initial data (16) for the backward heat equation has been generated with fifty modes in our applications later.

First of all, we want to emphasize that we solve the backward heat equation in a finite interval. For a solution to exist, following condition on initial data should be satisfied: “amplitude of the Fourier coefficient should decay faster than  $e^{-k^2}$  for a mode with wave number  $k$  for large  $k$  (see also Section 2.2 of [7])”. In Example 1, the cosine initial data has only one Fourier mode, thus the above condition is satisfied. It is easy to verify that the initial Gaussian data also satisfies this condition. For Example 3, the initial data  $v(x, 0)$  is generated using finite number of modes as mentioned above and hence this data also satisfies the above condition. Alternatively, one can also see that the initial data we use for these three examples satisfy the Picard criterion (see [7, p. 39]) which for the problem of backward heat conduction is  $\sum e^{(2k)^2} |f_k| < \infty$  (see [7, Section 1.5]).

For each of the examples above, using both the Euler and the Crank–Nicolson schemes, we compute numerical solutions  $\tilde{v}(x, T)$  from initial data  $v_0(x)$  using 14-digit accurate arithmetic. We do the experiments on  $[0, 1]$  for various grid sizes and up to various time levels  $t$ . Fig. 2(a) shows plots of exact and numerical solutions based on the cosine initial data (12) with  $k = 1$ . Fig. 2(b) shows similar plots but with cosine initial data having  $k = 6$ . In both figures we see that quality of solutions at time levels  $t = 3.5 \times 10^{-3}$  and  $t = 2 \times 10^{-3}$  shown in Figs. 2(a) and 2(b) respectively is acceptable. For time

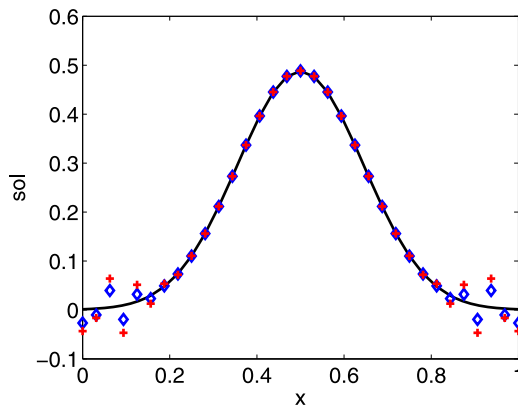


(a)  $k = 1, t = 3.5 \times 10^{-3}$ .

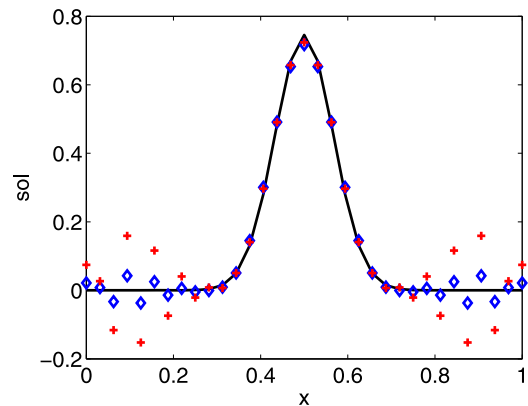


(b)  $k = 6, t = 2 \times 10^{-3}$ .

**Fig. 2.** Cosine initial data (12) (Example 1). Comparison of exact (solid line) and numerical solutions (Euler in diamonds and CN in plus) for different initial data. Results are with  $\Delta t = 10^{-4}$  and  $M = 33$ . Plus symbols and diamond symbols are on top of each other wherever the contrast between diamond and plus symbols are in question in the figure.



(a)  $\nu = 10^{-2}, t = 2 \times 10^{-1}$  and  $\Delta t = 5 \times 10^{-3}$ .



(b)  $\nu = 5 \times 10^{-3}, t = 8 \times 10^{-1}$  and  $\Delta t = 10^{-2}$ .

**Fig. 3.** Gaussian initial data (14) (Example 2). Comparison of exact (solid line) and numerical solutions (Euler in diamonds and CN in plus) for different initial data and  $M = 33$ . Plus symbols and diamond symbols are on top of each other wherever the contrast between diamond and plus symbols are in question in the figure.

levels beyond these the accuracy of solutions gradually deteriorates with increase in time of simulation due to growth of participating short waves present in the round-off and the truncation errors. The normalized  $L_2$  norm of the error between the exact solution  $v_e(., t)$  and the numerical solution  $v(., t)$  at time  $t$ , defined by

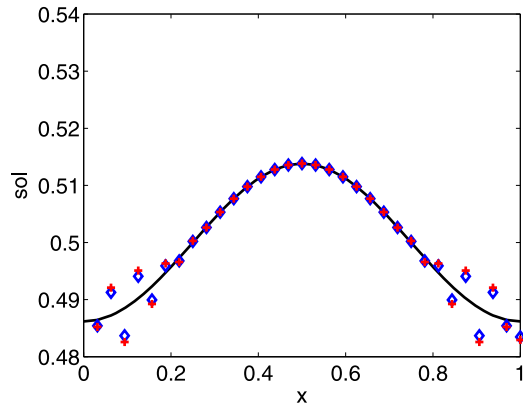
$$e_{L_2}(t) = \frac{\|v(., t) - v_e(., t)\|_2}{\|v_e(., t)\|_2},$$

is shown in Table 1 for both cosine initial data. Figs. 3(a), 3(b) and 4 show similar plots for Gaussian initial data (14) (two different values of  $\epsilon$ ) and square bump initial data (15) respectively. The normalized  $L_2$  error norms are shown in Table 1.

The evolution of the  $L_2$  errors for these three examples is shown in Fig. 5. As expected, it grows exponentially for both the Euler and the Crank–Nicolson numerical schemes. However, a slight difference of maximum value can be noticed between them at  $t = 10^{-2}$  where errors are the largest with Crank–Nicolson.

Next we show some results with noisy initial data. To generate noisy initial data for the three examples, a noise function is introduced into the initial condition of the backward problems as follows:

$$v^\delta(x, 0) = v(x, 0) \times (1 + \delta(x)), \tag{17}$$



$T_0 = 0.1, t = 3 \times 10^{-3}$  and  $\Delta t = 10^{-5}$ .

**Fig. 4.** Bump square data (15) (Example 3). Comparison of exact (solid line) and numerical solutions (Euler in diamonds and CN in plus) for  $M = 33$ . Plus symbols and diamond symbols are on top of each other wherever the contrast between diamond and plus symbols are in question in the figure.

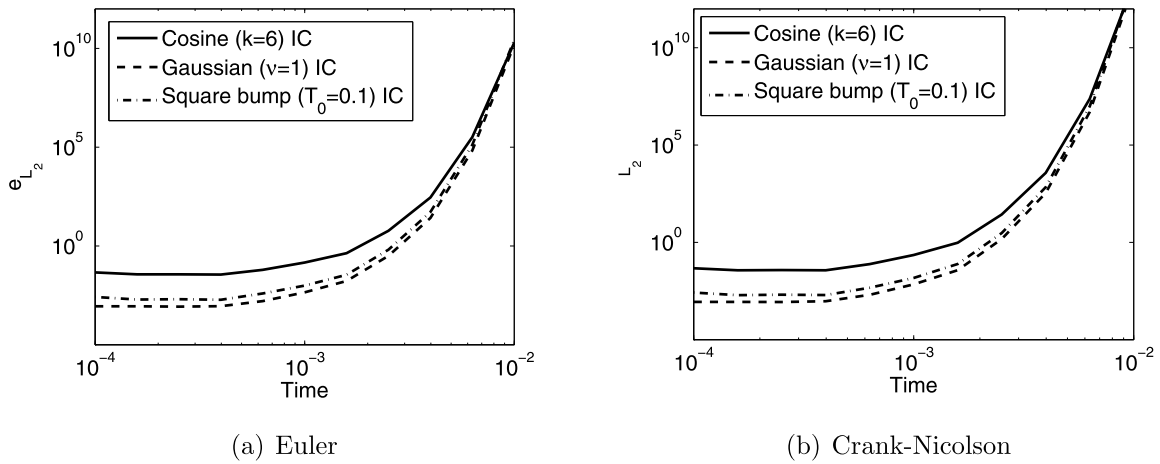


**Fig. 5.** Plot of  $L_2$  error versus time for three different examples without noise. For these plots  $M = 33, \Delta t = 10^{-4}$ .

**Table 1**  
Relative error norms without filtering.

IC	$\Delta t$	Time	Schemes	$e_{L_2}$
Cosine $k = 1$	$10^{-4}$	$t = 3.5 \times 10^{-3}$	Euler	$2.06 \times 10^{-2}$
			CN	$1.99 \times 10^{-1}$
Cosine $k = 6$	$10^{-4}$	$t = 2 \times 10^{-3}$	Euler	$1.45 \times 10^{-1}$
			CN	$4.5 \times 10^{-1}$
Gaussian $\nu = 10^{-2}$	$5 \times 10^{-3}$	$t = 2 \times 10^{-1}$	Euler	$5.41 \times 10^{-2}$
			CN	$9.85 \times 10^{-2}$
Gaussian $\nu = 5 \times 10^{-3}$	$10^{-2}$	$t = 8 \times 10^{-1}$	Euler	$8 \times 10^{-2}$
			CN	$2.88 \times 10^{-1}$
Example 3 $T_0 = 10^{-1}$	$10^{-5}$	$t = 3 \times 10^{-3}$	Euler	$4.08 \times 10^{-3}$
			CN	$5.04 \times 10^{-3}$

where  $\delta(x)$  is the noise generated using the MatLab function “rand” multiplied by a magnitude coefficient  $\delta_m$ :

$$\delta(x) = \delta_m \times \text{rand}(x). \tag{18}$$

For a fixed time  $t = 10^{-2}$ , Fig. 6 shows the plots of the  $L_2$  error as a function of the noise parameter  $\delta_m$  for both the Euler and the Crank–Nicolson schemes. In both cases, when the noise parameter is less than about  $10^{-4}$ , the error remains at a

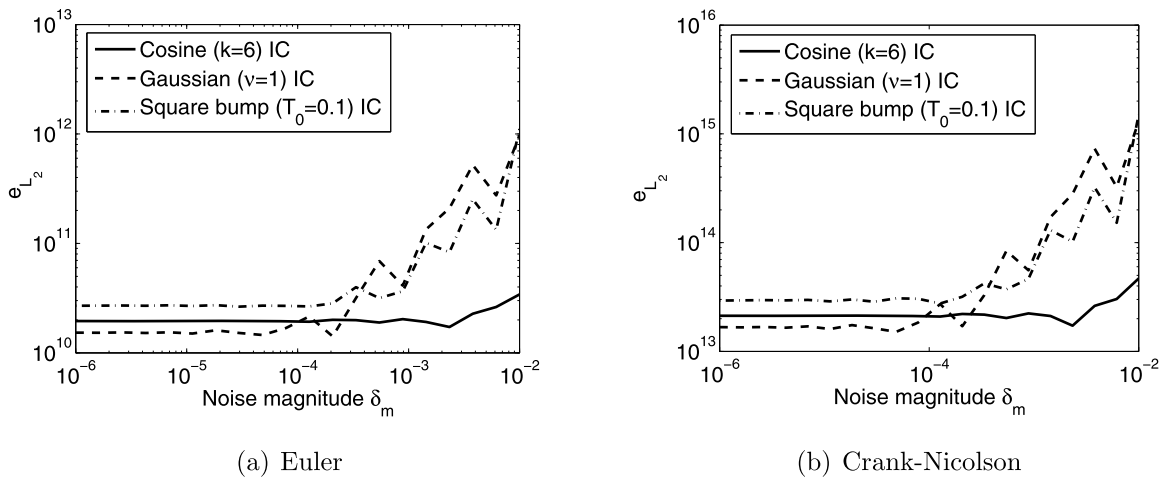


Fig. 6. Plot of  $L_2$  error at  $t = 10^{-2}$  versus noise parameter  $\delta_m$  for three different examples. For these plots  $M = 33$ ,  $\Delta t = 10^{-4}$ .

constant level ( $O(10^{10})$  for Euler and  $O(10^{13})$  for CN) corresponding to the values that can be observed without noise at  $t = 10^{-2}$  in Fig. 5. Above this value  $10^{-4}$  of the noise parameter, the error grows with an increase in the noise parameter for two of the three examples as seen in Fig. 6. It should be noted that with exactly the same numerical conditions and the noise parameter, error with the Crank–Nicolson scheme is three orders of magnitude larger than that with the Euler scheme.

### 3. Filtering technique

We have applied five different filters to control the spurious effects on the solution due to catastrophic growth of participating short wave components of the round-off and truncation errors. These low-pass filters, denoted as  $\Phi(k; k_c)$ , are applied on the Fourier spectrums  $a_k$  of the solution at certain time intervals (see Daripa [4] and text below for their proper applications). This results in the filtered spectrum  $a'_k$  and defined by

$$a'_k(k; k_c) = \Phi(k; k_c)a_k(k), \tag{19}$$

where  $a_k$  and  $a'_k$  denote respectively the unfiltered and filtered Fourier coefficients and  $k_c$  is a parameter, called cut off wave number, on which the filter depends (see below). First of these filters is the sharp filter  $\Phi_s$  defined by

$$\Phi_s(k) = \begin{cases} 1, & k \leq k_c, \\ 0, & k > k_c. \end{cases} \tag{20}$$

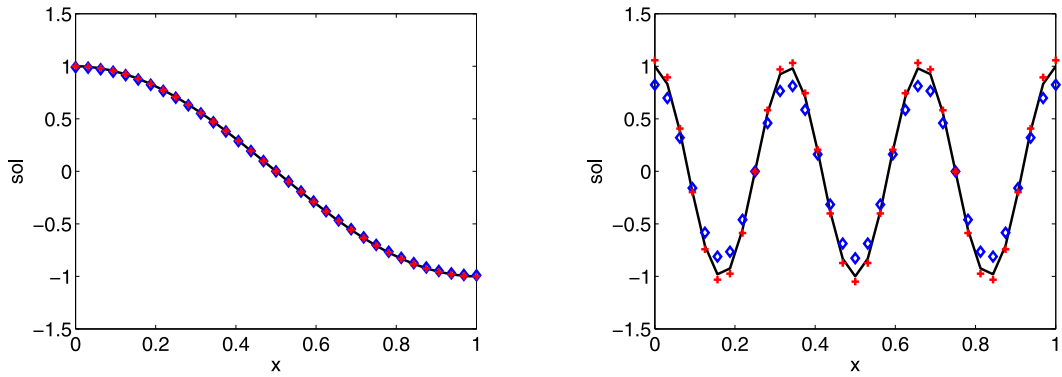
We have also applied another three filters described in Appendix A. Two of these  $\Phi_a(k)$  and  $\Phi_e(k)$  are  $C^\infty$  filters and the other three  $\Phi_i(k)$ ,  $i = 1, 2, 3$  have varying degrees of smoothness with smoothness of the filters increasing with index  $i$ . Below, figures and tables show numerical solutions for times much longer than otherwise possible without filters.

#### 3.1. Numerical results

Figs. 7(a), 7(b), 8(a), 8(b) and 9 compare exact solutions against the numerical solutions obtained using the sharp filter. Two ways of filtering have been used as it impacts on the result quality. On the one hand, the filter can be applied whenever the amplitude of the mode above the cut off ( $k_c$ ) exceeds  $10^{-5}$ : this method is called F1. On the other, the solution may be filtered every time steps: let us call it F2. The method of filtering has been reported in the results.

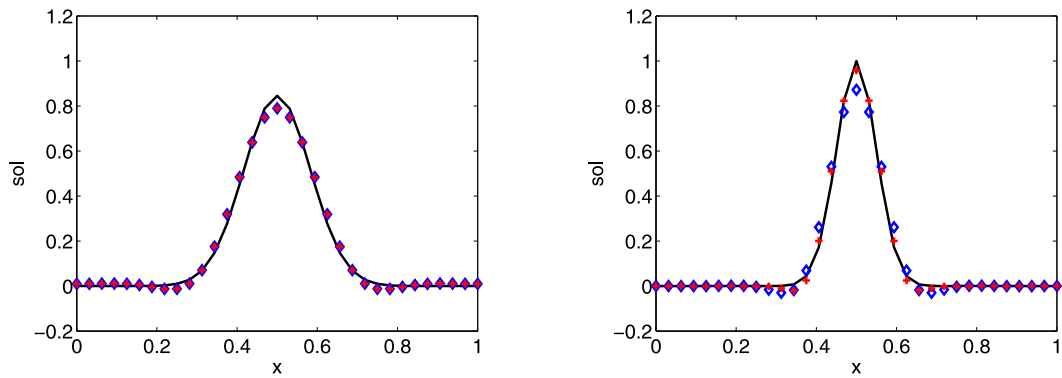
In the tested examples, choice of the filter shape does not affect noticeably the solutions in the three examples when plotted. However, cut off wave number  $k_c$  needs to be carefully selected in each case for it to be able to filter the spurious effects of computational (truncation and round-off errors) noise on the numerically constructed solutions.

Errors as a function of filter type and value of the cut off wave number  $k_c$  are shown in Table 2. In each case, the cut off wave number shown gives the reasonable good numerical solution. Data with other values of cut off wave numbers are not shown as these do not improve the solution. For a given precision (less than about  $5 \times 10^{-1}$ ), application of the filter enables computation of quality solutions for times more than what is otherwise possible without filtering. The most dramatic improvement occurs with the Example 1 with  $k = 1$ , where time increases from  $3.5 \times 10^{-3}$  to  $t = 1$  with the same



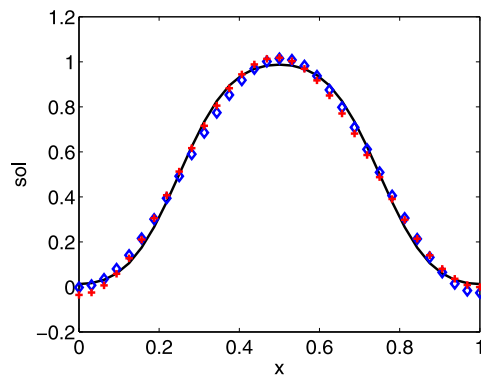
(a)  $k = 1, t = 1$  and  $\Delta t = 5 \times 10^{-3}$ . Filter cut off is  $k_c = 2$ . (b)  $k = 6, t = 10^{-2}$  and  $\Delta t = 4 \times 10^{-4}$ . Filter cut off is  $k_c = 7$

**Fig. 7.** Cosine initial data (12) (Example 1). Comparison of exact (solid line) and filtered numerical solutions (Euler in diamonds and CN in plus) for different initial data and  $M = 33$ . Plus symbols and diamond symbols are on top of each other wherever the contrast between diamond and plus symbols are in question in the figure.



(a)  $\nu = 10^{-2}, t = 0.9$  and  $\Delta t = 10^{-4}$ . Filter cut off is  $k_c = 10$ . (b)  $\nu = 5 \times 10^{-3}, t = 1$  and  $\Delta t = 5 \times 10^{-2}$ . Filter cut off is  $k_c = 16$ .

**Fig. 8.** Gaussian initial data (14) (Example 2). Comparison of exact (solid line) and filtered numerical solutions (Euler in diamonds and CN in plus) for different initial data and  $M = 33$ . Plus symbols and diamond symbols are on top of each other wherever the contrast between diamond and plus symbols are in question in the figure.

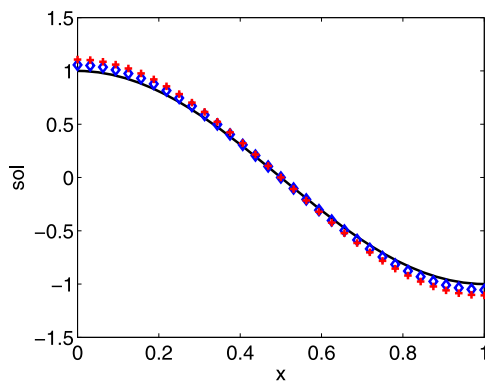


$T_0 = 0.1, t = 0.095, \Delta t = 10^{-4}$ . Filter cut off is  $k_c = 4$ .

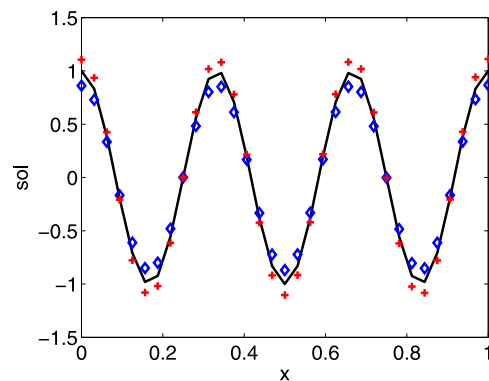
**Fig. 9.** Bump square data (15) (Example 3). Comparison of exact (solid line) and filtered numerical solutions (Euler in diamonds and CN in plus) for different initial data and  $M = 33$ . Plus symbols and diamond symbols are on top of each other wherever the contrast between diamond and plus symbols are in question in the figure.

**Table 2**  
Relative error norms with the three examples using filtering.

IC	$\Delta t$	Time	Cut off	Type	Schemes	$e_{L_2}$
Cosine $k = 1$	$5 \times 10^{-3}$	$t = 1$	$k_c = 2$	F2	Euler CN	$4.45 \times 10^{-2}$ $2.58 \times 10^{-2}$
Cosine $k = 6$	$4 \times 10^{-4}$	$t = 10^{-2}$	$k_c = 7$	F1	Euler CN	$1.72 \times 10^{-1}$ $5.45 \times 10^{-2}$
Gaussian $\nu = 10^{-2}$	$10^{-4}$	$t = 0.9$	$k_c = 10$	F1	Euler CN	$6.93 \times 10^{-2}$ $6.92 \times 10^{-2}$
Gaussian $\nu = 5 \times 10^{-3}$	$5 \times 10^{-2}$	$t = 1$	$k_c = 16$	F1	Euler CN	$1.36 \times 10^{-1}$ $6.33 \times 10^{-2}$
Example 3 $T_0 = 0.1$	$10^{-4}$	$t = 0.095$	$k_c = 4$	F1	Euler CN	$4.45 \times 10^{-2}$ $4.57 \times 10^{-2}$

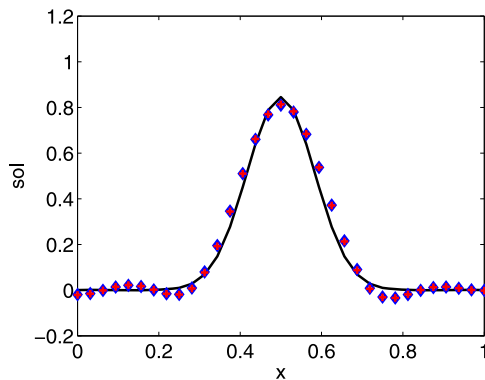


(a)  $k = 1, t = 1$  and  $\Delta t = 5 \times 10^{-3}$ . Filter cut off is  $k_c = 2$ .

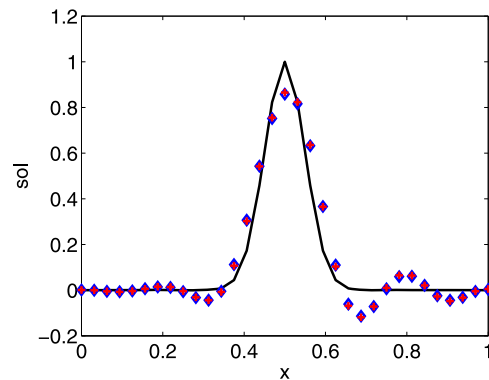


(b)  $k = 6, t = 10^{-2}$  and  $\Delta t = 4 \times 10^{-4}$ . Filter cut off is  $k_c = 7$ .

**Fig. 10.** Cosine initial data (12) (Example 1). Comparison of exact (solid line) and filtered numerical solutions (Euler in diamonds and CN in plus) for different initial data with noise and  $M = 33$ . Noise parameter  $\delta_m = 10\%$ . Plus symbols and diamond symbols are on top of each other wherever the contrast between diamond and plus symbols are in question in the figure.

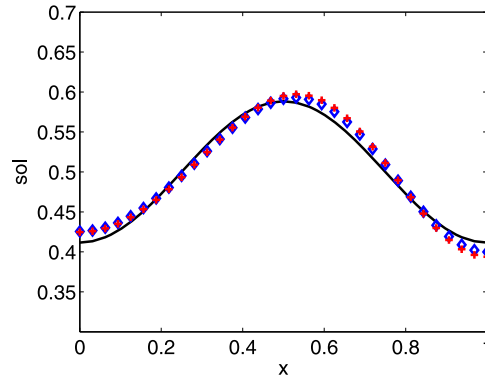


(a)  $\nu = 10^{-2}$  obtained at  $t = 0.9$  with  $\Delta t = 5 \times 10^{-3}$ . Filter cut off is  $k_c = 7$ .



(b)  $\nu = 5 \times 10^{-3}$  obtained at  $t = 1$  with  $\Delta t = 10^{-2}$ . Filter cut off is  $k_c = 10$ .

**Fig. 11.** Gaussian initial data (14) (Example 2). Comparison of exact (solid line) and filtered numerical solutions (Euler in diamonds and CN in plus) for different initial data with noise and  $M = 33$ . Noise parameter  $\delta_m = 10\%$ . Plus symbols and diamond symbols are on top of each other wherever the contrast between diamond and plus symbols are in question in the figure.



$T_0 = 0.1, t = 0.05, \Delta t = 10^{-4}$ . Filter cut off is  $k_c = 4$ .

**Fig. 12.** Bump square data (15) (Example 3). Comparison of exact (solid line) and filtered numerical solutions (Euler in diamonds and CN in plus) with noise and  $M = 33$ . Noise parameter  $\delta_m = 1\%$ . Plus symbols and diamond symbols are on top of each other wherever the contrast between diamond and plus symbols are in question in the figure.

**Table 3**  
Relative error norms with the three examples using filtering on noisy initial data.

IC	$\Delta t$	Time	Cut off	Type	Schemes	$e_{L_2}$
Cosine $k = 1$	$5 \times 10^{-3}$	$t = 1$	$k_c = 2$	F1	Euler	$5.55 \times 10^{-2}$
					CN	$1.07 \times 10^{-1}$
Cosine $k = 6$	$4 \times 10^{-4}$	$t = 10^{-2}$	$k_c = 7$	F2	Euler	$1.31 \times 10^{-1}$
					CN	$1.06 \times 10^{-1}$
Gaussian $\nu = 10^{-2}$	$5 \times 10^{-3}$	$t = 0.9$	$k_c = 7$	F2	Euler	$1.13 \times 10^{-1}$
					CN	$1.12 \times 10^{-1}$
Gaussian $\nu = 5 \times 10^{-3}$	$10^{-2}$	$t = 1$	$k_c = 10$	F2	Euler	$2.41 \times 10^{-1}$
					CN	$2.41 \times 10^{-1}$
Example 3 $T_0 = 0.1$	$10^{-3}$	$t = 0.05$	$k_c = 4$	F2	Euler	$1.67 \times 10^{-2}$
					CN	$2.11 \times 10^{-2}$

level of precision. Indeed, wavenumber of the mode being small, a small cut off may be applied and thus the contamination of the computation is delayed. The marginal enhancement is obtained with Example 2 with  $\nu = 5 \times 10^{-3}$  where simulation time for quality solution increases from  $8 \times 10^{-1}$  to 1. All the other cases are comprised between these extremes. The use of the method F1 of filtering has been necessary only with Example 1. In the other cases, no enhancement has been noticed so that the method F2 has been preferred because it provides the results faster.

Next we show results obtained with noisy initial data  $v^\delta(x, 0) = v(x, 0) \times (1 + \delta(x))$ , where  $\delta(x)$  denotes the noise presented in Eq. (18). In the case of Example 3 with noise, the magnitude of the coefficient had to be changed to  $\delta_m = 1\%$  as the value  $\delta_m = 10\%$  is comparable to the magnitude of the original initial function. Note that the function “rand” returns pseudo-random values drawn from a uniform distribution on the unit interval. Solutions analogous to those shown in Figs. 7(a), 7(b), 8(a), 8(b) and 9 but with noisy initial data are shown in Figs. 10(a), 10(b), 11(a), 11(b) and 12. Table 3 shows the various error norms with the sharp filter only because the results are similar with other filters. Similar to the case without noise, filtering helps improve the accuracy of the solution at any instant of time. The noise introduces high wavenumbers in the spectrum of the initial condition of the backward problem. They contaminate the solution initially but does so even more drastically to the solution at later times. Application of the filter at every time step (method F2) has been used to compute relatively accurate solutions at later times. In simulations with noise, the filter cut off  $k_c$  remains independent of the presence of noise.

Next we show for all three examples, two different types of plots of  $L_2$  error. In particular, Fig. 13 shows the  $L_2$  error against time for both the numerical schemes. For these simulations, no random noise has been added on the initial data. Next we show results of simulations from initial data with random noise added as per ansatz (17). Fig. 14 shows  $L_2$  error at a fixed time level as a function of the noise parameter  $\delta_m$  (see (18)). Comparison of Fig. 13 with Fig. 5 shows the effectiveness of the filters in limiting the contamination of the results by spurious growth of the high wave number modes of the round-off and discretization errors. On the other hand, comparison of Fig. 14 with Fig. 6 shows that noise levels  $\delta_m < 10^{-4}$  does not affect the  $L_2$  error for any of the examples in both the methods with this trend continuing even for some values of  $\delta_m$  higher than  $10^{-4}$  in some cases. However, as seen in these figures the error in Fig. 14 converges towards much smaller values than those obtained without filter as shown in Fig. 6. Growth of the error is clearly limited. But such

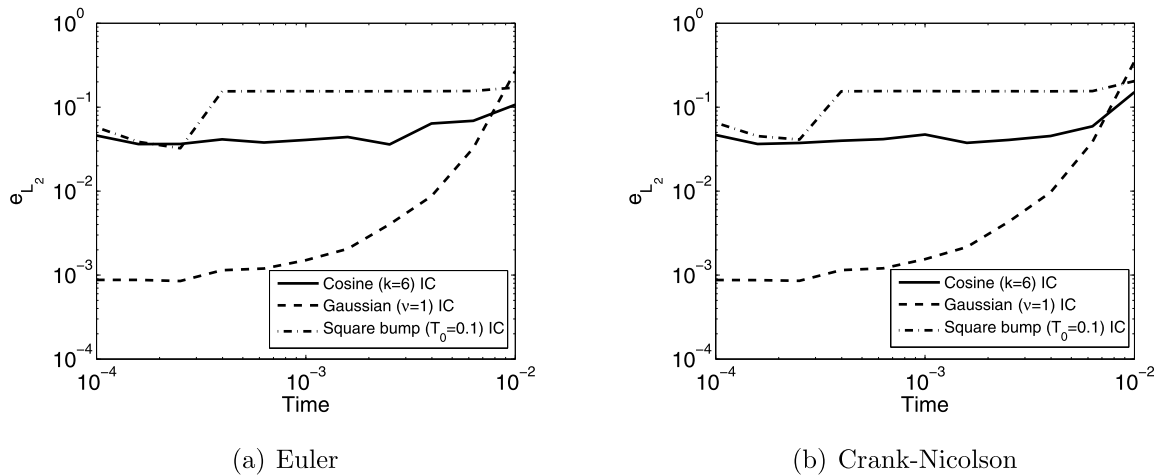


Fig. 13. Plot of  $L_2$  error versus time using filter for three different examples without noise. For these plots  $M = 33$ ,  $\Delta t = 10^{-4}$ . Filter cut off is  $k_c = 10$ , F2 method has been used where filter has been applied every 4th time step.

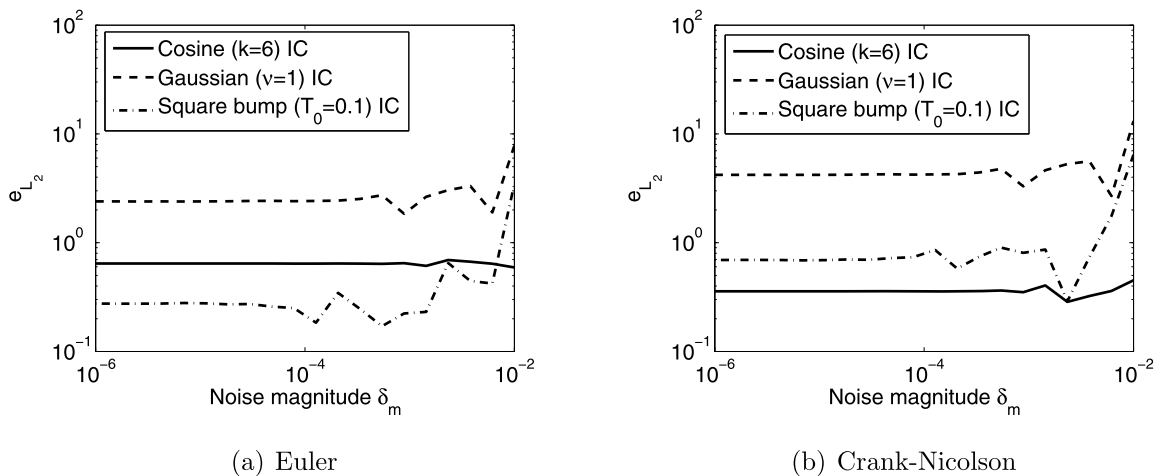


Fig. 14. Plot of  $L_2$  error at  $t = 10^{-2}$  versus the noise parameter using filter for three different examples. For these plots  $M = 33$ ,  $\Delta t = 10^{-4}$ . Filter cut off is  $k_c = 10$ , F2 type.

control has its limitation: the filter also removes the information that is required to retrieve fine scale features of solutions data when present and thus cannot be used to recover corners, discontinuities, etc. in the solutions if present.

4. Regularization technique

There exist different types of regularization techniques (see [1,18,16,8,23]). Here we regularize the backward heat equation by adding a fourth order term. The resulting problem is given by

$$\begin{cases} v_t + \nu v_{xx} + \epsilon v_{xxxx} = 0, & x \in \Omega = [0, 1], t \in [0, T], \\ v_x|_{\partial\Omega} = 0, & t \in [0, T], \\ v_{xxx}|_{\partial\Omega} = 0, & t \in [0, T], \\ v(x, 0) = \psi(x), & x \in \Omega. \end{cases} \tag{21}$$

The dispersion relation of this Eq. (21)<sub>1</sub> is given by

$$\omega = (\pi k)^2(\nu - \epsilon(\pi k)^2). \tag{22}$$

The most dangerous wave number  $k_d$  with the maximum growth rate  $\omega_{\max}$  and the wave number  $k^*$  of the neutral mode are given by

$$k_d = \frac{1}{\pi} \sqrt{\frac{\nu}{2\epsilon}}, \quad \omega_{\max} = \frac{\nu^2}{4\epsilon}, \quad k^* = \frac{1}{\pi} \sqrt{\frac{\nu}{\epsilon}}. \tag{23}$$

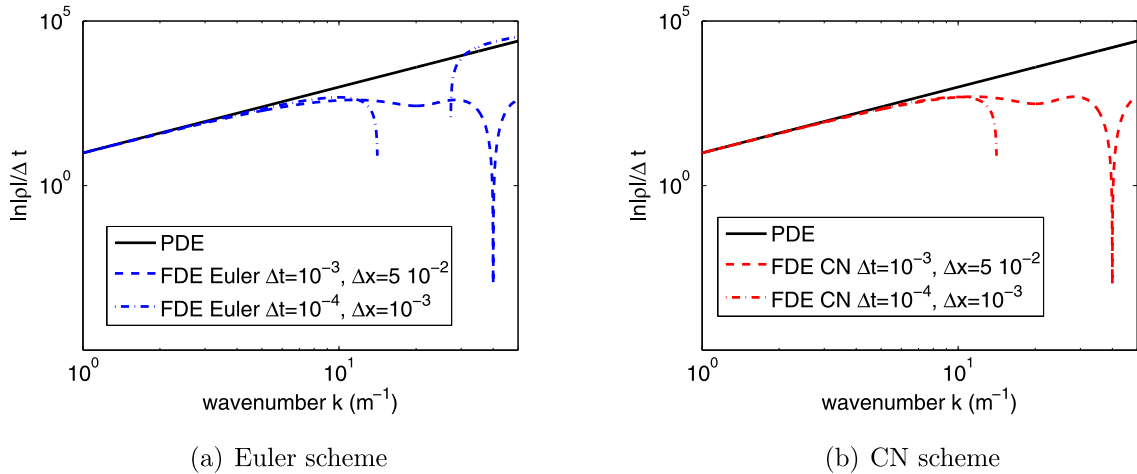


Fig. 15. Comparison of the exact ( $\omega$  versus  $k$ ) and numerical ( $|\rho|/\Delta t$  versus  $k$ ) dispersion relations for the regularized problem for several values of space and time steps. For these plots  $\nu = 1$  and  $k_d = 10$ .

An appropriate choice of small value for the regularizing parameter  $\epsilon$  can significantly curtail the spurious growth of short waves. We can see from the above formulas that we can equivalently treat  $k_d$  or  $k^*$  as regularizing parameter instead of  $\epsilon$  since value of  $\epsilon$  is automatically chosen if we choose either  $k_d$  or  $k^*$ . Next we discuss the schemes to be used for solving the above regularized problem.

4.1. Euler and CN schemes

**Euler scheme.** The finite difference equation for the regularized Eq. (21) is

$$\frac{D_t^+ v_m^n}{\Delta t} = -\nu \frac{D_x^+ D_x^- v_m^n}{\Delta x^2} - \epsilon \frac{D_x^+ D_x^- D_x^+ D_x^- v_m^n}{\Delta x^4}, \quad \forall m \neq \{1, M\}, \quad \forall n > 2. \tag{24}$$

For numerical construction of the accurate solutions, it is also necessary to choose appropriate values of  $\Delta x$  and  $\Delta t$  so that numerical and exact dispersion relations do not deviate too much from each other over a range of participating wave numbers. Using the ansatz  $v_m^n = \rho^n e^{i\xi m}$  (where  $\rho = e^{\beta \Delta t}$  and  $\xi = k\pi \Delta x$ ) in the finite difference equation (24) yields the dispersion relation

$$\rho = 1 + 4r \sin^2\left(\frac{\xi}{2}\right) - 16\mu \sin^4\left(\frac{\xi}{2}\right), \tag{25}$$

where  $\mu = \frac{\epsilon \Delta t}{\Delta x^4}$ . Fig. 15(a) compares the exact (see Eq. (22)) and the numerical (see Eq. (25)) dispersion relations for several choices of parameter values. This figure shows that optimal step sizes are  $\Delta x = 10^{-4}$  and  $\Delta t = 10^{-3}$  when  $\nu = 1$  and  $k_d = 10$ . Note that with this set of parameters, the dispersion relation seems to be discontinuous in the range  $[12, 26]$  of  $k$ . In fact, this is due to the representation in log scale of the function that reaches a value close to zero.

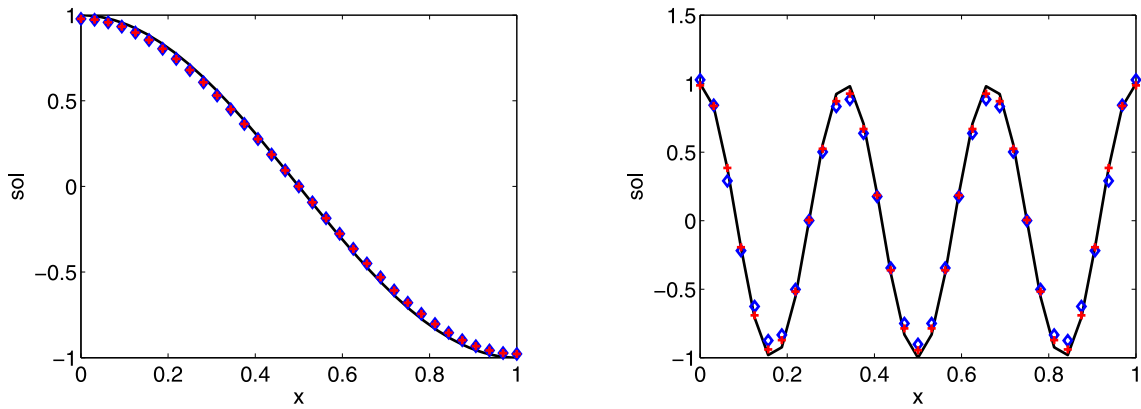
**Crank–Nicolson scheme.** The finite difference equation for the above regularized equation is

$$\frac{D_t^+ v_m^n}{\Delta t} = -\frac{\nu}{2\Delta x^2} (D_x^+ D_x^- v_m^{n+1} + D_x^+ D_x^- v_m^n) - \frac{\epsilon}{2\Delta x^4} (D_x^+ D_x^- D_x^+ D_x^- v_m^{n+1} + D_x^+ D_x^- D_x^+ D_x^- v_m^n). \tag{26}$$

For dispersion relation, the same ansatz for  $v_m^n$  as in the Euler scheme is inserted in the finite difference equation (26) of the Crank–Nicolson scheme. This yields the following dispersion relation:

$$\rho = \frac{1 + 2r \sin^2\left(\frac{\xi}{2}\right) - 8\mu \sin^4\left(\frac{\xi}{2}\right)}{1 - 2r \sin^2\left(\frac{\xi}{2}\right) + 8\mu \sin^4\left(\frac{\xi}{2}\right)}. \tag{27}$$

Fig. 15(a) compares the exact (see Eq. (22)) and the numerical (see Eq. (25)) dispersion relations for several choices of parameter values. This figure shows that the optimal step sizes are  $\Delta x = 10^{-4}$  and  $\Delta t = 10^{-3}$  when  $\nu = 1$  and  $k_d = 10$ . Since the plot is in log scale, note that sometimes the growth factor is undefined in a defined range of wavenumber because some values of  $\rho$  are less than zero.



(a)  $k = 1, t = 10^{-1}$  and  $\Delta t = 10^{-5}$ . Results are with  $k_d = 4$  (for both Euler and CN). (b)  $k = 6, t = 5 \times 10^{-3}$  and  $\Delta t = 10^{-3}$ . Results are with  $k_d = 16$  (for Euler) and  $k_d = 10$  (for CN).

**Fig. 16.** Cosine initial data (12) (Example 3). Comparison of exact (solid line) and regularized numerical solutions (Euler in diamonds and CN in plus) for different initial data and  $M = 33$ . Plus symbols and diamond symbols are on top of each other wherever the contrast between diamond and plus symbols are in question in the figure.

4.2. Numerical boundary conditions

Regularization introduces a fourth order term in the equation and a second boundary condition at each boundary (see (21)). The fourth order derivative term is evaluated by finite central differences using five points:

$$v_{xxxx}(x_i, t_j) = \frac{v_{i+2}^j - 4v_{i+1}^j + 6v_i^j - 4v_{i-1}^j + v_{i-2}^j}{\Delta x^4}. \tag{28}$$

Because of this term in the discrete approximation of the regularized equation at the interior grid points, solutions at two points outside the domain, namely  $v_{-1}^j$  and  $v_{M+1}^j$ , are required. This is done the following way using the second boundary condition (21). The third order derivative term  $v_{xxx}$  is approximated to second order accuracy as

$$v_{xxx}|_{x=0} = \frac{-\frac{3}{2}v(-\Delta x) + 5v(0) - 6v(\Delta x) + 3v(2\Delta x) - \frac{1}{2}v(3\Delta x)}{\Delta x^3} + O(\Delta x^2).$$

Using the boundary condition  $v_{xxx} = 0$  and the third order accurate approximation (4) in the above formula, we obtain third order accurate formulae

$$v(-\Delta x) \simeq \frac{4v(\Delta x) + 8v(2\Delta x) - 3v(3\Delta x)}{9}, \tag{29}$$

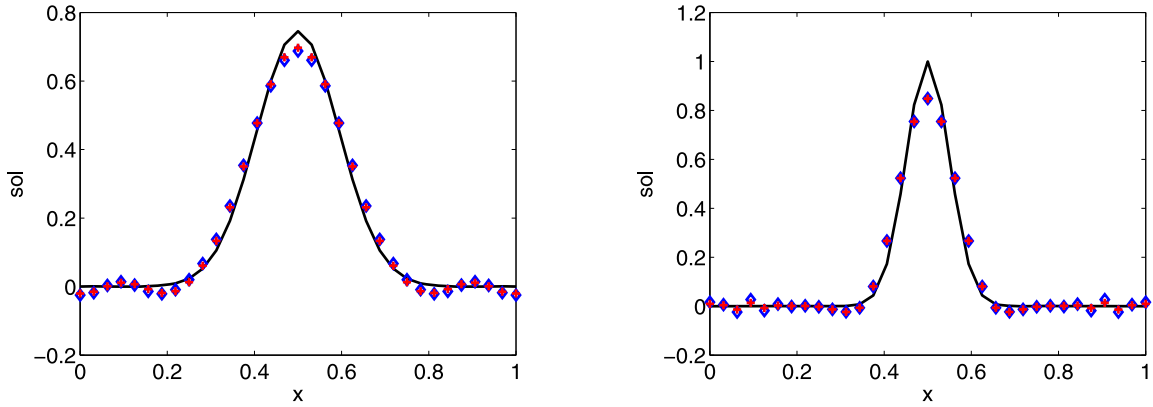
and similarly at  $x = 1$  (using Eq. (5))

$$v(1 + \Delta x) \simeq \frac{4v(1 - \Delta x) + 8v(1 - 2\Delta x) - 3v(1 - 3\Delta x)}{9}. \tag{30}$$

4.3. Numerical results

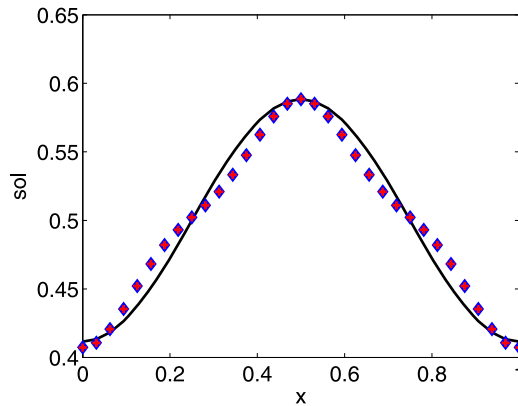
Figs. 16(a), 16(b), 17(a), 17(b) and 18 compare the numerical solutions against the exact solutions of the regularized problem. The normalized  $L_2$  error norms are shown in Table 4. The regularized Euler and CN schemes do not give the best results for the same parameter set. The parameters for which we obtain the best results for each of these scheme are mentioned in the caption of the figures and are also reported in Table 4. These numerical results confirm that under a given tolerance of error, the simulation time can be increased significantly using regularization.

Finally, we present results of regularization of the backward problem subject to initial conditions with noise:  $v^\delta(x, 0) = v(x, 0) \times (1 + \delta(x))$  (see Eq. (18)). The same settings as presented in the section dedicated to the filtering, e.g., the magnitude of  $\delta = 10\%$  for all examples except for Example 3 where it is 1%, are used for these simulation with regularization. Plots are shown in Figs. 19(a), 19(b), 20(a), 20(b) and 21. Table 5 recaps the error norms. As expected, noise prevents from reaching as large simulation time as with pure initial data. As before, we present in Fig. 22 the error growth as a function of time using regularization. For these simulations, no random noise has been added on the initial data. The sensitivity of the solutions to noise has also been found to be interesting which is shown in Fig. 23. Comparing Fig. 22 with Fig. 5 and Fig. 23 with Fig. 6



(a)  $\nu = 10^{-2}$ ,  $t = 0.8$  and  $\Delta t = 5 \times 10^{-2}$ . Results are with  $k_d = 11$  (for Euler) and  $k_d = 10$  (for CN). (b)  $\nu = 5 \times 10^{-3}$ ,  $t = 1$  and  $\Delta t = 10^{-2}$ . Results are with  $k_d = 28$  (for Euler) and  $k_d = 24$  (for CN).

**Fig. 17.** Gaussian initial data (14) (Example 2). Comparison of exact (solid line) and regularized numerical solutions (Euler in diamonds and CN in plus) for different initial data and  $M = 33$ . Plus symbols and diamond symbols are on top of each other wherever the contrast between diamond and plus symbols are in question in the figure.



$T_0 = 0.1$ ,  $t = 0.05$ ,  $\Delta t = 10^{-5}$ . Results are with  $k_d = 6$  (for both Euler and CN)

**Fig. 18.** Bump square data (15) (Example 3). Comparison of exact (solid line) and regularized numerical solutions (Euler in diamonds and CN in plus) for  $M = 33$ . Plus symbols and diamond symbols are on top of each other wherever the contrast between diamond and plus symbols are in question in the figure.

**Table 4**  
Relative error norms with regularization.

IC	$\Delta t$	Time	$k_d$	Schemes	$e_{L_2}$
Cosine $k = 1$	$10^{-5}$	$t = 10^{-1}$	$k_d = 4$	Euler	$3.18 \times 10^{-2}$
				CN	$3.17 \times 10^{-2}$
Cosine $k = 6$	$10^{-3}$	$t = 5 \times 10^{-3}$	$k_d = 16$ $k_d = 10$	Euler	$9.81 \times 10^{-2}$
				CN	$4.81 \times 10^{-2}$
Gaussian $\nu = 10^{-2}$	$5 \times 10^{-2}$	$t = 0.8$	$k_d = 11$ $k_d = 10$	Euler	$8.63 \times 10^{-2}$
				CN	$7.6 \times 10^{-2}$
Gaussian $\nu = 5 \times 10^{-3}$	$10^{-2}$	$t = 1$	$k_d = 28$ $k_d = 24$	Euler	$1.53 \times 10^{-1}$
				CN	$1.51 \times 10^{-1}$
Example 3 $T_0 = 10^{-1}$	$10^{-5}$	$t = 5 \times 10^{-2}$	$k_d = 6$	Euler	$2.11 \times 10^{-2}$
				CN	$2.12 \times 10^{-2}$

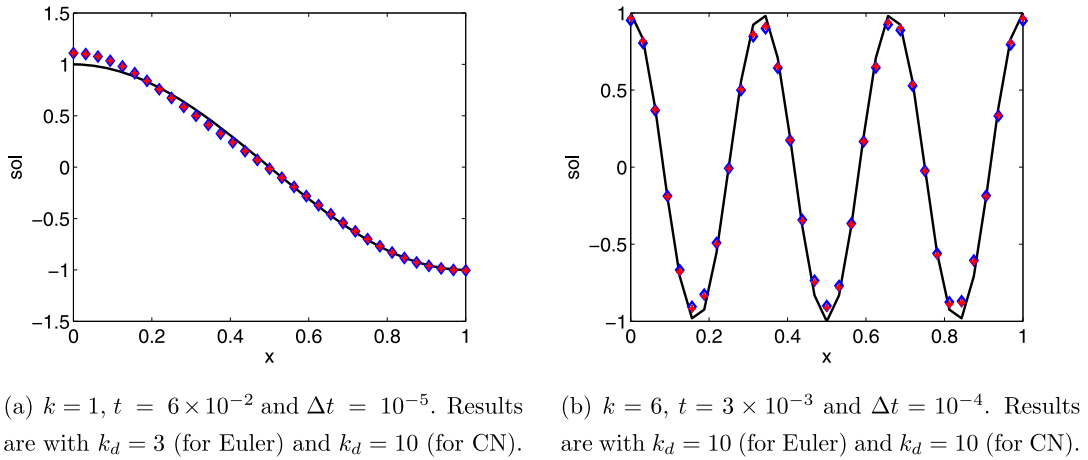


**Fig. 19.** Cosine initial data (12) (Example 1). Comparison of exact (solid line) and regularized numerical solutions (Euler in diamonds and CN in plus) for different initial data with noise and  $M = 33$ . Noise parameter is  $\delta_m = 10\%$ . Plus symbols and diamond symbols are on top of each other wherever the contrast between diamond and plus symbols are in question in the figure.

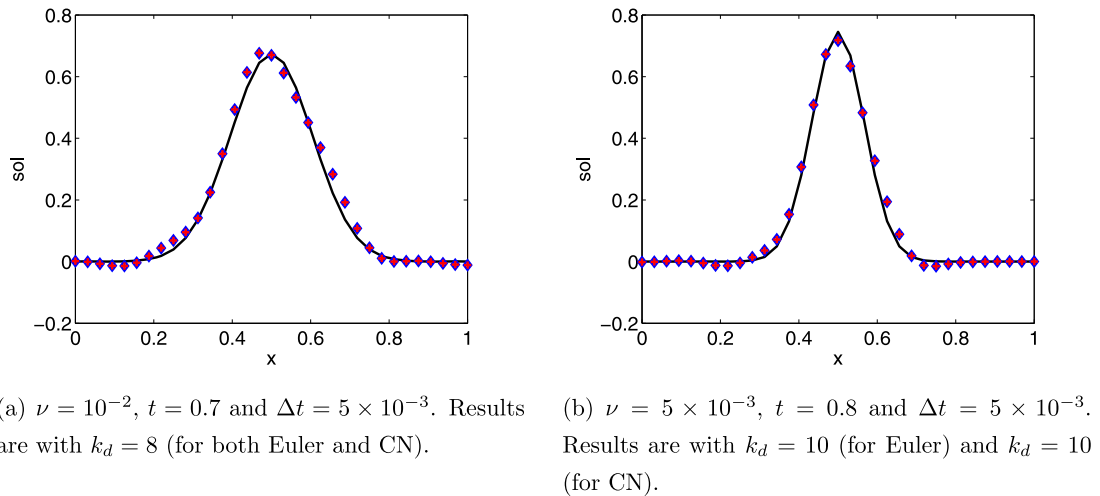


**Fig. 20.** Gaussian initial data (14) (Example 2). Comparison of exact (solid line) and regularized numerical solutions (Euler in diamonds and CN in plus) for different initial data with noise and  $M = 33$ . Noise parameter  $\delta_m = 10\%$ . Plus symbols and diamond symbols are on top of each other wherever the contrast between diamond and plus symbols are in question in the figure.

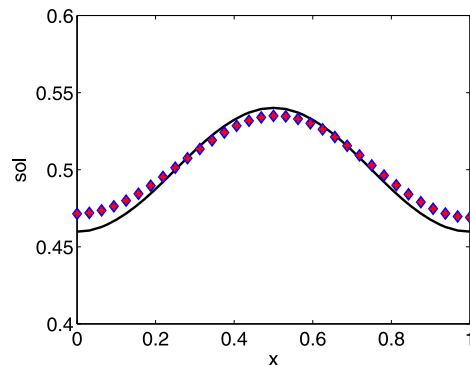
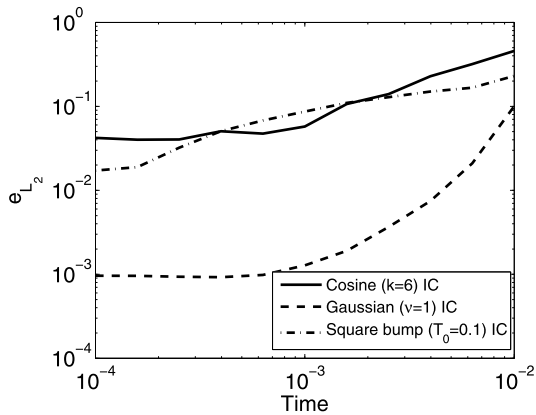


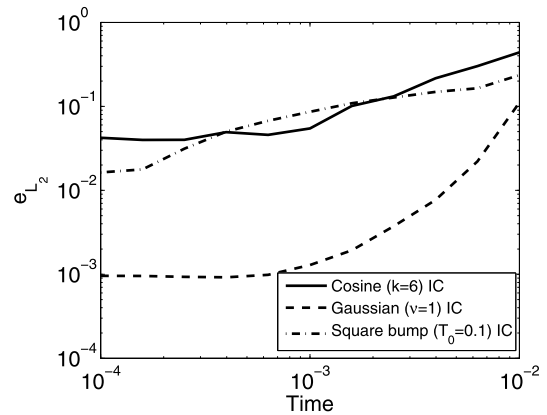
**Fig. 21.** Bump square data (15) (Example 3). Comparison of exact (solid line) and regularized numerical solutions (Euler in diamonds and CN in plus) with noise for  $M = 33$ . Noise parameter is  $\delta_m = 1\%$ . Plus symbols and diamond symbols are on top of each other wherever the contrast between diamond and plus symbols are in question in the figure.

**Table 5**  
Relative error norms with regularization on noisy initial conditions.

IC	$\Delta t$	Time	$k_d$	Schemes	$e_{L_2}$
Cosine $k = 1$	$10^{-5}$	$t = 8 \times 10^{-2}$	$k_d = 3$	Euler	$5.9 \times 10^{-2}$
				CN	$5.91 \times 10^{-2}$
Cosine $k = 6$	$10^{-4}$	$t = 3 \times 10^{-3}$	$k_d = 12$	Euler	$8.26 \times 10^{-2}$
				CN	$7.13 \times 10^{-2}$
Gaussian $\nu = 10^{-2}$	$5 \times 10^{-3}$	$t = 0.7$	$k_d = 8$	Euler	$8.54 \times 10^{-2}$
				CN	$8.55 \times 10^{-2}$
Gaussian $\nu = 5 \times 10^{-3}$	$5 \times 10^{-3}$	$t = 0.8$	$k_d = 10$	Euler	$8.02 \times 10^{-2}$
				CN	$7.91 \times 10^{-2}$
Example 3 $T_0 = 10^{-1}$	$10^{-5}$	$t = 2 \times 10^{-2}$	$k_d = 3$	Euler	$1.21 \times 10^{-2}$
				CN	$1.21 \times 10^{-2}$

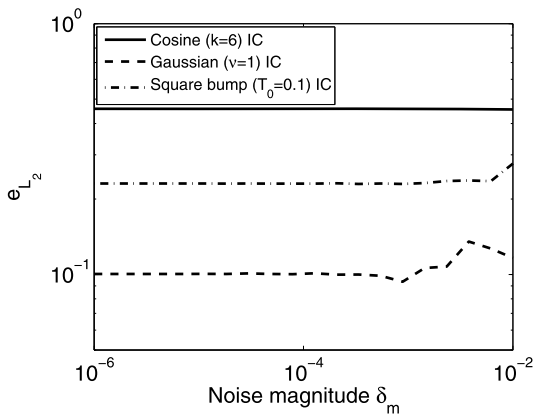


(a) Euler

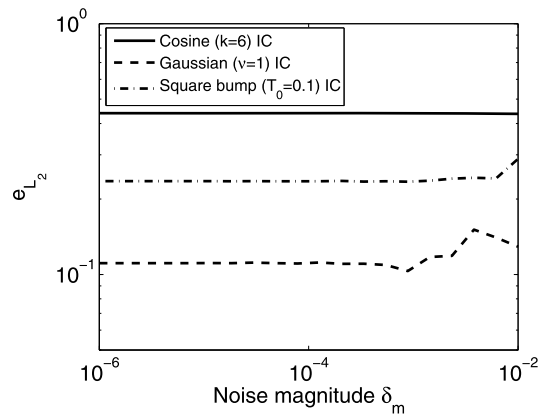


(b) Crank-Nicolson

**Fig. 22.** Plot of  $L_2$  error versus time using regularization for three different examples without noise. For these plots  $M = 33$ ,  $\Delta t = 10^{-4}$ . Regularization parameter is given by  $k_d = 10$ .



(a) Euler



(b) Crank-Nicolson

**Fig. 23.** Plot of  $L_2$  error at  $t = 10^{-2}$  versus the noise parameter  $\delta_m$  using regularization for three different examples. For these plots  $M = 33$ ,  $\Delta t = 10^{-4}$ . Regularization parameter is given by  $k_d = 10$ .

respectively, it is observed that regularization limits growth of the error with or without noise. Moreover, its effect is fully comparable to that of the filter (see Figs. 13 and 14).

For our purposes below, value of the regularization parameter  $\epsilon$  for which the  $L_2$  error is least will be called optimal value, denoted by  $\epsilon^*$ , of the parameter  $\epsilon$ . The choice of the optimal value  $\epsilon^*$  certainly depends on the noise parameter  $\delta_m$

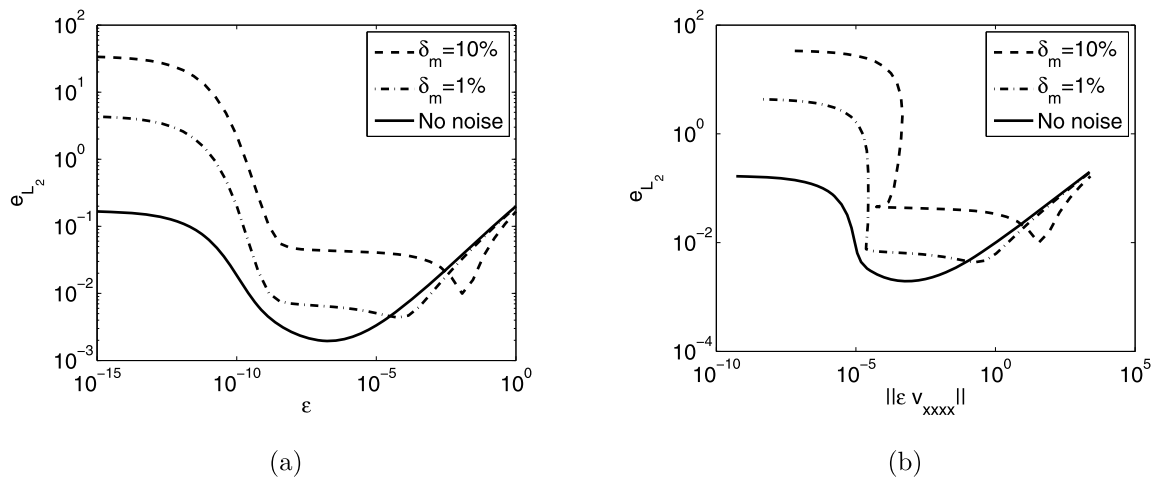


**Fig. 24.** Plot of  $L_2$  error at  $t = 2 \times 10^{-3}$  versus the regularization parameter  $\epsilon$  with the cosine initial data ( $k = 1$ ) for three values of the noise parameter  $\delta_m$ . For these plots  $\Delta t = 10^{-5}$  and  $M = 33$ .

which is a measure of signal to noise ratio modulo some constant depending on the examples. A strategy that will allow selection of  $\epsilon^*$  in dependency of the noise parameter  $\delta_m$  is certainly helpful. However, it is not clear how to do this a priori. To get some insight into how to do this even a posteriori, plots of  $L_2$  error are shown against the regularization parameter  $\epsilon$  and the residual norm ( $\|\epsilon \times v_{xxxx}\|$ ) in Figs. 24(a) and 24(b) respectively. The results are shown with CN scheme only and for the first example only because general trends of the plots for other combinations of the two methods and the three examples of this paper are similar. The plots in Fig. 24(a) resemble U-curves and those in Fig. 24(b) resemble L-curves. It is worth mentioning here that  $L_2$  errors and the residual norms were computed for decreasing values of the regularization parameter  $\epsilon$  and then these plots were done. Therefore, it should be understood that the parameter  $\epsilon$  decreases as any of the L-curves (including the one which looks more like a U for no noise case in Fig. 24(b)) is traced from right to left.

We see from the U-curves that both, the minimal value of  $L_2$  error (corresponding to  $\epsilon^*$ ) and the optimal value  $\epsilon^*$  decrease monotonically with decreasing values of the noise parameter  $\delta_m$ . From the L-curves, same inference is drawn about the dependency of  $L_2$  error on the noise. However, notice that the effect of  $\epsilon$  decreasing away from the optimal value  $\epsilon^*$  has much more dramatic effect on the  $L_2$  error than on the residual. In the presence of noise,  $L_2$  error increases rapidly with hardly any change in the residual (the L-part of the L-curves). Therefore, either of the curves can be used for choosing the optimal value  $\epsilon^*$ .

In general, smaller the magnitude of the noise, smaller the optimal value of the regularization parameter  $\epsilon^*$ . The value of  $\epsilon^*$  seems to remain constant when the noise parameter reaches a value less than 0.01% (figure is not shown here). Indeed, for such a value of  $\delta_m < 0.01\%$  and such time level, the error is no longer affected by the noise in agreement with the observation made in Fig. 6. As seen in the U-curves, for optimal choice  $\epsilon^*$  of the regularizing parameter with noise level  $\delta_m < 0.01\%$  in the initial data, the regularized solution approximates the exact one having an  $L_2$  error of the order of  $O(10^{-3})$ . In concluding this section, we want to emphasize that the discussion here on U- and L-curves is based on plots made from data obtained at a specific time level. More research is needed (which will be a topic of research in the future) to determine, even a posteriori, the optimal value of the regularizing parameter in dependency of time of simulation.

## 5. Discussion and conclusion

Two stable ways of computing solutions of backward heat equation, namely filtering (direct filtering of short waves) and regularization techniques (structural perturbation of the heat equation), have been proposed and discussed for their proper implementation. For each of these ways of computing stable solutions, two finite difference methods, namely the Euler method and the Crank–Nicolson (CN) method, for solving the associated initial boundary value problem have been devised. These schemes have been analyzed. In particular, (numerical) dispersion relations for these two numerical schemes associated with each of the two initial boundary value problems arising in filtering and regularizing techniques respectively have been derived.

Appropriate choice of parameters so that numerical dispersion relations well approximate the exact dispersion relations of the PDEs over the range of participating wave numbers is one of the important factors in devising stable ways of computing the numerical solutions of the backward heat equation. This has been one of the hallmarks of the success of these methods which has been exemplified in this paper with adequate number of examples. Another important factor has been to apply the filter and set the level of the filter appropriately which is partly guided by severity of ill-posedness and partly by trial and error. We have shown here that in this way, we are able to compute stable solutions for times longer than

otherwise possible. The methods are new. It will be interesting to see whether these results compare favorably or not with other existing methods [2,3,10,12,14,15,21,24] which is a topic of future research.

The filtering and regularization methods are used to obtain smooth approximate solutions of ill-posed problems. The filtering methods have been applied here in a way that can provide good approximate smooth solutions but falls short of providing singular solutions such as the ones with corners and discontinuities. Such corners and discontinuities are smoothed out in the solutions obtained by the way the filtering techniques are applied here. Singular solutions can be obtained by better applications of the filtering techniques which is difficult to apply in general because the application process involves in part science and in part art (see [13]). In the regularization technique, we have provided the  $U$ -curve criterion for optimal choice of the regularizing parameter a posteriori. This optimal value is shown to decrease with decreasing noise level.

**Acknowledgements**

This paper has been made possible by a NPRP grant to one of the authors (Prabir Daripa) from the Qatar National Research Fund (a member of The Qatar Foundation) and by a SCAT grant to the other two authors (Fabien Ternat and Oscar Orellana). One of the authors (Fabien Ternat) thanks the Department of Mathematics at Texas A&M University for making his one month long summer visit to Dr. Daripa possible and enjoyable. He also thanks the Department of Mathematics at Universidad Tecnica Federico Santa Maria, Valparaiso, Chile for making his research under SCAT grant possible. We would also like to thank immensely the reviewers for their very constructive and insightful criticisms which have helps up to improve the paper. The statements made herein are solely responsibility of the authors.

**Appendix A. Definition of the filters used**

We have applied five filters one of which is described in the main body of the text and the rest four are defined below:

1. Arctan filter  $\Phi_a(k)$ :

$$\Phi_a(k) = \frac{1}{\pi} \arctan(-10^4(k - k_c)) + 0.5. \tag{31}$$

2. Three polynomial filters  $\Phi_i(k)$ : smoothness of the sharp filter defined in the main body of the text can be improved by considering polynomial functions  $g_i$  (see Daripa [4]):

$$\Phi_i(k, p) = \begin{cases} 1, & k \leq k_c, \\ 1 - g_i(\hat{k}), & k_c < k < k_2, \\ 0, & k \geq k_2, \end{cases} \tag{32}$$

where  $\hat{k} = \frac{k - k_c}{k_2 - k_c}$ . The smoothing functions are defined respectively by:

$$g_1(x) = x, \quad 0 < x < 1, \tag{33}$$

$$g_2(k) = \begin{cases} \frac{9}{2}x^3, & 0 < x \leq \frac{1}{3}, \\ 9x^3 + \frac{27}{2}x^2 - \frac{9}{2}x + \frac{1}{2}, & \frac{1}{3} < x \leq \frac{2}{3}, \\ 1 - \frac{9}{2}(1-x)^3, & \frac{2}{3} < x < 1, \end{cases} \tag{34}$$

$$g_3(k) = \begin{cases} \frac{625}{24}x^5, & 0 < x \leq \frac{1}{5}, \\ -\frac{625}{6}x^5 + \frac{3125}{24}x^4 - \frac{625}{12}x^3 + \frac{125}{12}x^2 - \frac{25}{24}x + \frac{1}{24}, & \frac{1}{5} < x \leq \frac{2}{5}, \\ \frac{625}{4}x^5 - \frac{3125}{8}x^4 + \frac{4375}{12}x^3 - \frac{625}{4}x^2 + \frac{775}{24}x - \frac{21}{8}, & \frac{2}{5} < x \leq \frac{3}{5}, \\ 1 + \frac{625}{6}(1-x)^5 - \frac{3125}{24}(1-x)^4 + \frac{625}{12}(1-x)^3 - \frac{125}{12}(1-x)^2 + \frac{25}{24}(1-x) - \frac{1}{24}, & \frac{3}{5} < x \leq \frac{4}{5}, \\ 1 - \frac{625}{24}(1-x)^5, & \frac{4}{5} < x < 1. \end{cases} \tag{35}$$

These filters have varying degree of smoothness and how to apply these have been exemplified in gory detail in Daripa [4].

## References

- [1] K.A. Ames, L.E. Payne, Asymptotic behavior for two regularizations of the Cauchy problem for the backward heat equation, *Mathematical Models and Methods in Applied Sciences* 8 (1998) 187–202.
- [2] L.D. Chiuwacowsky, H.F. De Campo Velho, Different approaches for the solution of a backward heat conduction problem, *Inverse Problem Engineering* 11 (2003) 471–494.
- [3] D.T. Dang, H.T. Nguyen, Regularization and error estimates for nonhomogeneous backward heat problems, *Electronic Journal of Differential Equations* 2006-04 (2006) 1–10.
- [4] P. Daripa, Some useful filtering techniques for ill-posed problems, *Journal of Computational and Applied Mathematics* 100 (1998) 161–171.
- [5] P. Daripa, H. Wei, A numerical study of an ill-posed Boussinesq equation arising in water waves and nonlinear lattices: Filtering and regularization techniques, *Applied Mathematics and Computation* 101 (1999) 159–207.
- [6] J.J. Douglas, T.M. Gallie, An approximate solution of an improper boundary value problem, *Duke Mathematical Journal* 26 (1959) 339–347.
- [7] H. Engl, M. Hanke, A. Neubauer, *Regularization of Inverse Problems*, Kluwer Academic Publishers, 2000.
- [8] C.-L. Fu, X.-T. Xiong, Z. Qian, Fourier regularization for a backward heat equation, *Journal of Mathematical Analysis and Applications* 331 (2007) 472–480.
- [9] K. Höllig, Existence of infinitely many solutions for a forward backward heat equation, *Transactions of the American Mathematical Society* 279 (1983) 299–316.
- [10] H. Houde, Y. Dongsheng, A non overlap decomposition method for the forward-backward heat equation, *Journal of Computational and Applied Mathematics* 159 (2003) 35–44.
- [11] F. John, Numerical solution of the equation of heat conduction for preceding times, *Annali di Matematica Pura et Applicata Series IV* 40 (1955) 129–142.
- [12] L. Kentaro, Numerical solution of backward heat conduction problems by a high order lattice-free finite difference method, *Journal of the Chinese Institute of Engineers* 27 (2004) 611–620.
- [13] R. Krasny, A study of singularity formation in a vortex sheet by the point-vortex approximation, *Journal of Fluid Mechanics* 167 (1986) 65–93.
- [14] D. Krawczyk-Stando, M. Rudnicki, Regularization parameter selection in discrete ill-posed problems – the use of the  $u$ -curve, *International Journal of Applied Mathematics and Computer Sciences* 17 (2007) 157–164.
- [15] N.S. Mera, The method of fundamental solutions for the backward heat conduction problem, *Inverse Problems in Science and Engineering* 13 (2005) 65–78.
- [16] N.S. Mera, L. Elliot, D.B. Ingham, An inversion method with decreasing regularization for the backward heat conduction problem, *Numerical Heat Transfer, Part B* 42 (2002) 215–230.
- [17] W. Miranker, A well posed problem for the backward heat equation, *Proceedings of the American Mathematical Society* 12 (1961) 243–247.
- [18] W.B. Muniz, F.M. Ramos, H.F. De Campos Velho, Entropy- and Tikhonov-based regularization techniques applied to the backwards heat equation, *Computers and Mathematics with Applications* 40 (2000) 1071–1084.
- [19] J. Nash, Continuity of solutions of parabolic and elliptic equations, *American Journal of Mathematics* 80 (1958) 931–954.
- [20] C. Pucci, Sui problemi di Cauchy non “ben posti”, *Atti Accademia Nazionale dei Lincei. Rend. Classe di Scienze Fisiche, Matematiche e Naturali* 18 (1955) 473–477.
- [21] A. Qian, C.-L. Fu, R. Shi, A modified method for a backward heat conduction problem, *Applied Mathematics and Computation* 185 (2007) 564–573.
- [22] I. Seidman, Optimal filtering for the backward heat equation, *SIAM Journal of Numerical Analysis* 33 (1996) 162–170.
- [23] G. Teschke, M. Zhariy, M.J. Soares, A regularization of nonlinear diffusion equations in a multiresolution framework, *Mathematical Methods in the Applied Sciences* 31 (2008) 575–587.
- [24] X.-T. Xiong, C.-L. Fu, A. Qian, Two numerical methods for solving a backward heat conduction problem, *Applied Mathematics and Computation* 179 (2006) 370–377.